Journal of Power Sources 196 (2011) 5438–5445

Contents lists available at ScienceDirect

Journal of Power Sources

journal homepage: www.elsevier.com/locate/jpowsour

Effect of Pt-loaded carbon support nanostructure on oxygen reduction catalysis

Dustin Banham[a], Fangxia Feng[a], Tobias Fürstenhaupt[b], Katie Pei[a], Siyu Ye[c], Viola Birss[a,*]

[a] Department of Chemistry, University of Calgary, 2500 University Drive NW, Calgary, AB T2N 1N4, Canada
[b] Microscopy and Imaging Facility, University of Calgary, Health Sciences Centre B129, 3330 Hospital Drive NW, Calgary, AB T2N 4N1, Canada
[c] Ballard Power Systems, 9000 Glenlyon Parkway, Burnaby, BC V5J 5J8, Canada

ARTICLE INFO

Article history:
Received 25 January 2011
Accepted 12 February 2011
Available online 21 February 2011

Keywords:
Proton exchange membrane fuel cell
Oxygen reduction reaction catalysts
Nanostructure
Ordered mesoporous carbon
Colloid-imprinted carbon
Transmission electron tomography

ABSTRACT

This work demonstrates the impact of the nanostructure (pore size, wall thickness and wall crystallinity) of several carbon materials on their performance as oxygen reduction reaction (ORR) catalyst supports in PEM fuel cell applications. Two different mesoporous carbons [a surfactant-templated ordered mesoporous carbon (OMC) with 1.6 and 3.3 nm pores, and a silica colloid-imprinted carbon (CIC) with a 15 nm pore size], selected as being the most active in their class, were compared with microporous Vulcan Carbon. After loading with 20 and 40% Pt, both 3D transmission electron microscopy and electron tomography revealed that the Pt nanoparticles reside inside the majority of the pores of the OMC and CIC, but are located only on the outer surface of the VC particles. ORR performance studies on a rotating glassy carbon disc electrode in O_2-saturated 0.5 M H_2SO_4 showed that the Pt-loaded CIC outperforms both Pt-loaded OMC and VC. This is attributed to the higher electronic conductivity (due to the thicker and more crystalline walls, seen by both X-ray diffraction and thermogravimetric analysis) and facilitated mass transport in the larger pores of the CIC support.

1. Introduction

Fuel cells are devices that very efficiently convert chemical energy directly into electrical energy through electrochemical reactions, without the generation of pollutants, such as NO_x, SO_x, or particulates. One of the leading types of fuel cells is the proton exchange membrane fuel cell (PEMFC), which operates at relatively low temperatures (~80 °C), resulting in a rapid start up time and making it very well suited for transportation and portable applications. When operated on pure H_2 and air, the only product formed in a PEMFC is pure H_2O.

In order for the electrochemical conversion of H_2 (at the anode) and O_2 (at the cathode) into water to proceed in a PEMFC, catalytic sites that are accessible to protons, electrons, and reactant gases are required. This is accomplished by using porous, electronically conducting electrodes that also contain a proton conducting phase, such as Nafion™. In PEMFCs, Pt is used as both the anode and cathode catalyst, with the oxygen reduction reaction (ORR) being the rate limiting process. While PEMFCs have many advantages, the high cost of Pt makes it essential to disperse it as nanoparticles in order to increase the surface to area ratio, thus maximizing its usage. Currently, this is achieved by depositing Pt nanoparticles onto a conducting, high surface area, porous carbon support material.

Vulcan XC-72R carbon (VC) is currently the most widely employed catalyst support for PEMFC applications, as it is relatively crystalline and hence has good electronic conductivity. Although VC also has a reasonably high surface area (~220 $m^2\ g^{-1}$), it is primarily a microporous material, with pores < 2 nm in diameter. These pores are too small to accommodate Pt nanoparticles of the optimal size (2–4 nm) [1] and thus the Pt particles reside primarily on the outer surface of the VC particles, making them prone to dislodgement and/or agglomeration. Further, the micropores in VC are likely too small [2] to be accessible to the Nafion ionomer (distributed throughout the catalyst layer to provide proton-transfer pathways), with its hydrophilic pockets in the 1–5 nm range, depending on the degree of hydration [2,3]. Another problem with VC support materials is that they can suffer severely from corrosion during start-up and shut-down of PEMFCs [4].

In order to overcome these problems, recent efforts have been focussed on synthesizing mesoporous (2–50 nm pore diameter [5]) carbon support materials. This includes ordered mesoporous carbons (OMCs), materials that are typically prepared using an amine surfactant to first template an ordered mesoporous silica (OMS) structure, which then templates the formation of the OMC. These OMCs have a very narrow pore size distribution, tuneable between 2 and 7 nm in diameter [6] and exhibit among the highest double layer capacitances yet reported for carbon [7].

* Corresponding author. Tel.: +1 403 220 6432; fax: +1 403 289 9488.
E-mail address: birss@ucalgary.ca (V. Birss).

0378-7753/$ – see front matter © 2011 Elsevier B.V. All rights reserved.
doi:10.1016/j.jpowsour.2011.02.034

The first literature report regarding the use of Pt-loaded surfactant-templated OMCs as ORR catalysts was quite promising [8], likely related to the small Pt particle size (~2.5 nm) achieved on the high surface area of OMCs (>1000 $m^2 g^{-1}$), even at high (50 wt% Pt) loadings. Using TEM electron tomography, Chang et al. [9] showed that the Pt nanoparticles on an OMC containing pores ~5 nm in diameter [9] (formed using a meso-structured cellular SiO_2 foam) are uniformly distributed throughout the full porous structure of the OMC. However, for a Pt-loaded OMC with a pore size of ~3.5 nm, electron tomography [10] showed that the majority of the Pt particles reside on the outer surface, with only a few Pt nanoparticles found inside the OMC pores. Notably, the morphological results reported in these papers were never linked to the electrochemical performance of the catalysts.

Other groups have shown that Pt/OMCs perform very well at low currents, but display mass transport limitations at higher currents [11–13]. It is therefore possible that the pores of the OMCs may be large enough to accommodate Pt, but not Nafion [14]. Also, it has been shown that, when sucrose is used as the OMC precursor, the resulting structure is relatively amorphous and thus expected to be more susceptible to corrosion than more graphitic supports [15]. Despite these challenges, recent work [16] has continued to focus on optimizing OMC materials as catalyst supports for PEM fuel cell applications, primarily due to the small Pt particles size and homogeneous Pt distribution reported for these carbons.

Another type of mesoporous carbon (colloid-imprinted carbon, CIC) has been recently developed by the colloidal imprinting of a mesophase pitch carbon [6], giving pore diameters > 7 nm in size. Since the pitch is comprised of an aromatic napthalene polymer, the resulting support (after carbonization) is relatively graphitic and hence quite conductive, similar to VC. When a CIC (26 nm pores) was loaded with Pt, the preliminary ORR activity was very good relative to similarly loaded VC and no mass transport limitations were seen at high currents [17]. Despite these promising results, to date, only two published Communications have examined the ORR at Pt-loaded CICs [17,18]. It is clear that a direct comparison of the ORR performance at Pt-loaded VC, the OMCs, and these new CICs, carried out within a single laboratory (using the same ink preparation and deposition methods, and the same performance evaluation tools) is necessary.

Therefore, this work involves the first-time direct comparison of the ORR activity at these three categories of Pt-loaded (20 and 40 wt%) carbon supports, all treated and evaluated in the same manner. Using high-resolution TEM electron tomography, it is shown that the improved kinetic performance of both the Pt-loaded CIC and OMC supports (vs. Pt-loaded VC) in the activation region, obtained from rotating disc studies, is due to their smaller Pt nanoparticle size (higher catalytic area) and more uniform Pt particle distribution. However, the Pt/CIC catalyst gives the best ORR activity, overall, at all potentials, due to the larger pores and thicker, more crystalline walls of the CIC support, thus minimizing mass transport losses.

2. Experimental

2.1. Ordered mesoporous carbon (OMC) synthesis

The preparation of the ordered mesoporous carbons (OMCs) followed a procedure reported previously [19], except that HMS (a wormhole structure) silica was used, as opposed to SBA-15 (a hexagonal structure) [20]. Further details of the synthesis can be found in previous work from our group [7]. Briefly, the chain length (n) of the surfactant templating agent ($C_nH_{2n+1}NH_2$) was varied between 8 and 16, making four different ordered mesoporous silica (OMS) structures. These were then each filled with sucrose and carbonized, with the silica subsequently removed by refluxing in 2.5 wt% NaOH.

2.2. Colloid-imprinted carbon (CIC) synthesis

The synthesis of the colloid-imprinted carbon (CIC) support material (15 nm pores) was based on a procedure previously reported by Li and Jaroniec [6], where mesophase pitch (MP) carbon pellets (Mitsubishi, Japan) were ground in a mortar and pestle and then filtered using a 270 mesh sieve. One gram of the ground MP powder was dispersed in 20 mL of EtOH/H_2O (60:40 v/v) and 20 mL of a 40 wt% colloidal silica suspension in H_2O (Ludox-HS-40 12 nm diameter silica colloids, on average) were then added drop-wise with vigorous stirring. The temperature of the stirred mixture was raised to 50 °C to promote solvent evaporation, after which the remaining carbon/silica composite was heated under N_2 to 360 °C at a ramp rate of 5 °C min^{-1}. The sample was then held at 360 °C for an additional 2 h, cooled to 220 °C, and then held there for 10 h. The material was then allowed to cool to room temperature (RT) under a continuous flow of N_2, followed by carbonization at 900 °C (5 °C min^{-1}) for 2 h and then cooling to RT under a constant N_2 flow. Finally, 1 g of the carbon/silica composite was refluxed in 100 mL of 3 M NaOH for 24 h to remove the silica, washed with water to achieve a neutral pH, dried at 120 °C, and then ground again using a mortar and pestle, forming the CIC powder.

2.3. Pt loading of carbon supports

The CIC, OMC, and VC (Vulcan XC-72R carbon, Cabot) powders were all loaded with Pt (either 20 or 40 wt%) using a wet-impregnation method [8], employing $H_2PtCl_6{\cdot}6H_2O$ as the Pt precursor and H_2 as the reducing agent. In this approach, 0.67 g (20 wt% Pt) and 1.78 g (40 wt% Pt) of $H_2PtCl_6{\cdot}6H_2O$, dissolved in 2 mL of acetone, were added drop-wise to 1 g of carbon with vigorous stirring. The sample was then dried at 60 °C overnight. The $H_2PtCl_6{\cdot}6H_2O$ was reduced by heating the sample under H_2 from room temperature (RT) to 300 °C over a period of 2 h, kept at 300 °C for 2 h under N_2 to remove any adsorbed H_2, and then allowed to cool to RT.

2.4. Material characterization

X-ray powder diffraction (XRD) patterns were obtained using a Rigaku Multiflex X-ray diffractometer (Department of Geology, University of Calgary), using Cu K_α radiation (λ = 0.15406 nm). The operating conditions were 40 kV and 20 mA and the data were processed with Jade software (Version 6.5). Thermogravimetric analysis (TGA) was performed on a Setaram TAG16 at a heating rate of 10 °C min^{-1} from RT to 800 °C in 20% O_2/He.

Nitrogen adsorption–desorption isotherms were collected at −196 °C using a Micromeritics Tristar 3000 analyzer. Prior to analysis, samples were out-gassed in N_2 at 250 °C for 4 h. The specific surface area was obtained using the Brunauer–Emmett–Teller (BET) plot ($0.05 < P/P^0 < 0.30$), where P and P^0 are the partial pressure and vapour pressure of the adsorbate gas, respectively. The total pore volumes were calculated at $P/P^0 = 0.99$, while the pore size distribution curves were calculated from the adsorption branch of the isotherm using the Barrett–Joyner–Halenda (BJH) mode.

All transmission electron microscopy (TEM) work was carried out on a Tecnai TF20 G2 FEG-TEM (FEI, Hillsboro, OR, USA) with a Fischione 2040 Dual-Axis Tomography Holder (Fischione Instruments, Export, PA, USA). The catalysts were suspended in ethanol and sonicated for 5 min. A drop of this suspension was placed on one side of a TEM Slot Grid (1 mm × 2 mm) that was covered with a ~40 nm thin continuous Formvar film (EMS, Hatfield, PA, USA) and left to dry for several minutes. Colloidal gold particles (10 nm)

were placed on the other side of the grid to serve as fiducial markers. Finally, a thin carbon coating was applied to both sides of the grid for mechanical stabilization and to reduce electric charging in the microscope. All TEM images were captured on a 1024 × 1024 pixel Gatan GIF 794 CCD (Gatan, Pleasanton, CA, USA). Dual axis TEM tomography was carried out by taking one image every degree for a range between 130 and 145° with the program SerialEM [21]. The tomographic reconstruction was done by weighted back-projection with the IMOD software package [22,23]. The same software was used for visualization and analysis.

2.5. Electrochemical evaluation of catalysts

0.01 g of the Pt/C powder was dispersed into 0.4 g of a 1.0 wt% Nafion/isopropanol solution (for the OMC and CIC-supported catalysts) or a 1.0 wt% Nafion/EtOH solution (for VC-supported catalyst) and sonicated for at least 25 min. An Eppendorf pipette was used to deposit 14 μl of the ink onto a glassy carbon rotating disc (RDE) working electrode (WE) and dried at room temperature. The mass of the deposited ink aliquot was typically 10–11.5 mg (Mettler Toledo AB204 analytical balance), resulting in a Pt/C catalyst loading of 0.25–0.30 mg.

The catalysts were then evaluated in a three-electrode cell containing a platinised Pt mesh counter electrode, a reversible hydrogen reference electrode (RHE), and the 7 mm diameter glassy carbon RDE, cast with the catalyst film. Cyclic voltammetry (CV) was carried out using a Solartron 1287 potentiostat in conjunction with an EG&G PARC 175 function generator. The cell solution was 0.5 M H_2SO_4, purged with vigorous bubbling of either N_2 (Praxair 99%) or O_2 (Praxair medical grade).

All catalyst layers were first electrochemically cleaned by scanning between −0.05 and 1.7 V at 100 mV s^{-1} for 20 cycles, followed by CV analysis (0.05–1.1 V vs. RHE) in a N_2-saturated aqueous solution with no electrode rotation. The ORR electrochemistry was then evaluated at 10 mV s^{-1} in an O_2-saturated cell using a Pine analytical rotor (Model ASR-2). The baseline CVs in N_2-saturated conditions were then subtracted from the CVs collected under aerated conditions to remove the non-Faradiac component of the current. All CV data were collected using Chart 5 by PowerLab.

3. Results and discussion

3.1. Selection of mesoporous carbons for comparison

Because high surface area supports are known to promote excellent Pt nanoparticle dispersion [8] and thus would be expected to give the highest ORR activity, an ordered mesoporous carbon (OMC) having the highest possible surface area was sought in this work. Fig. 1 shows that, the longer the surfactant chain used to synthesize the ordered mesoporous silica (OMS) template, the higher the resulting OMC surface area, based on N_2 sorption measurements. These results are consistent with the recently reported [7] trends in the double layer capacitance of this series of OMCs. Therefore, the OMC prepared from the $C_{16}H_{33}NH_2$-templated OMS (the maximum length surfactant available), having a BET-determined surface area of 1570 m^2 g^{-1} (Table 1), was chosen for comparison in the present work.

The CIC examined in the present study was chosen based on parallel work in our group, showing that a Pt-loaded CIC (15 nm pores) outperforms other CICs with both smaller and larger [18] pore sizes. Since one of the main goals of the present work was to demonstrate the benefits of CICs vs. conventional OMCs, and also to compare against VC as a Pt nanoparticle support material, the most active CIC (15 nm pore diameter) was selected for the present study. Table 1 shows that VC possesses the lowest surface area (of the three carbons) of 220 m^2 g^{-1}, typical of what has been reported previously by others [24], while the CIC has a surface area of 330 m^2 g^{-1}.

Table 1
Selected physical properties of carbon support materials prior to Pt loading.

Carbon support	BET surface area (±10 m^2 g^{-1})	Pore size[b] (nm)	Pore volume (mL g^{-1})
VC	220	<2	0.70
OMC[a]	1570	1.6 (65%), 3.3 (35%)	1.10
CIC	330	15	1.20

[a] Formed using $C_{16}H_{33}NH_2$-templated OMS.
[b] Calculated using the BJH (Barrett–Joyner–Halenda) model.

3.2. Carbon support material pore sizes

Table 1 gives the carbon pore sizes (determined from the N_2 sorption data), which match closely with what was expected [7,18] from the two synthesis routes used to prepare them. Based on the pore sizes, VC is seen to be primarily microporous [25,26], while the OMC and CIC supports are clearly mesoporous in nature. The OMC mesostructure is bimodal, with 65% of its internal volume taken up by pores 1.6 nm in diameter and 35% by pores 3.3 nm in diameter [7]. The reason for the bimodal nature of the OMC may be the partial filling of the silica template, in successive steps, during the synthesis of OMC, as explained in more detail in an earlier paper [7].

3.3. Carbon support crystallinity

XRD (Fig. 2) was used to determine the graphitic character of the carbon materials (prior to Pt loading), primarily as a more crystalline (more graphitic) structure is associated with higher electronic conductivity [15,27]. Indeed, we have recently shown [18] that the resistance of the carbon support can be one of the most important factors limiting cathode performance in PEM fuel cells. As well, it is generally accepted that graphitic carbon should be more resistant to electrochemical oxidation (reaction (1)) than amorphous carbon [15,27]. By comparing the width of the graphite (0 0 2) peak at $2\theta \sim 24°$ (Fig. 2), it is seen that OMC, synthesized using sucrose, contains much smaller graphitic domains (broader peak) than VC (narrower peak). The OMC therefore has an amorphous structure with a low degree of graphitization, expected to correlate with a higher electronic resistance and a

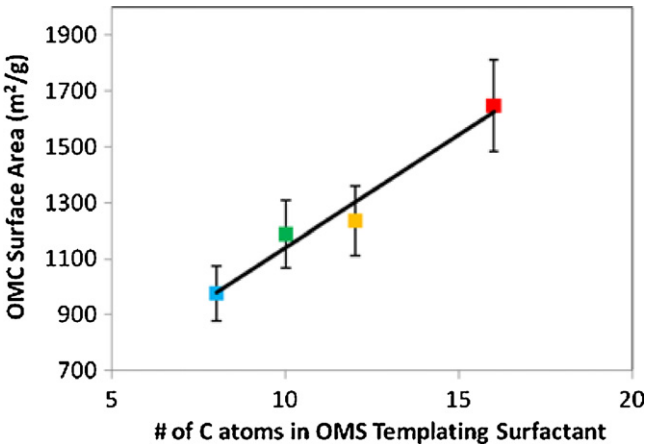

Fig. 1. Surface area of OMCs vs. number of carbon atoms in the surfactant used to prepare the OMS templates from which the OMCs are derived.

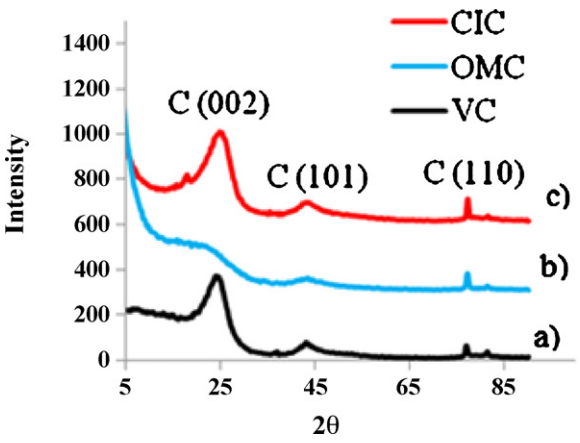

Fig. 2. XRD patterns of (a) VC, (b) OMC, and (c) CIC before Pt loading.

greater susceptibility to oxidation, relative to graphitic carbon [14].

Compared to the OMC, the graphite (0 0 2) peak for the CIC is much sharper, similar to VC. This increased graphitic character is a significant advantage of these CICs vs. the OMC supports. It should be noted that both the OMC and CIC were carbonized at the same temperature (900 °C). Heat treating CICs to still higher (>1000 °C) temperatures during carbonization could further increase their graphitic domain sizes, while maintaining their mesoporous structure [28]. In the case of the OMCs, however, these higher temperatures could have a detrimental effect on the structure of the porous network [28].

To confirm these differences in the carbon crystallinity, Fig. 3 shows the TGA results for the three carbon materials, all with a 20 wt% Pt loading, when heated at 10 °C min^{-1} in air up to a maximum temperature of 800 °C. It is seen that VC and CIC have a similar resistance to air oxidation, while OMC is more susceptible, the same trends as seen by XRD analysis (Fig. 2). Indeed, it is known that amorphous carbon will be oxidized more readily than graphitic carbon under TGA conditions [29,30] This can be rationalized using thermodynamic arguments, based on Eq. (2), showing that, the more positive the ΔG_f value for carbon, the more favourable ΔG_{rxn} (the more negative E°) will be.

$$C + 2H_2O \rightleftharpoons CO_2 + 4H^+ + 4e^- \quad E^\circ = 0.207\,V \tag{1}$$

$$\Delta G_{rxn} = [\Delta G_f(CO_2) + 4\Delta G_f(H^+)] - [2\Delta G_f(H_2O) + \Delta G_f(C)] \tag{2}$$

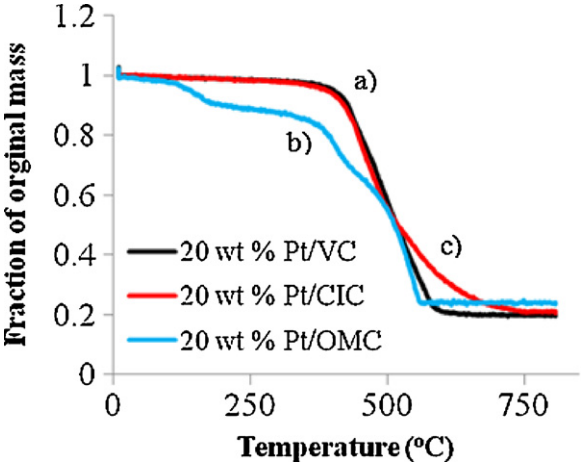

Fig. 3. TGA of 20 wt% Pt-loaded (a) VC, (b) OMC, and (c) CIC, all at a heating rate of 10 °C min^{-1} from RT to 800 °C in 20% O_2/He.

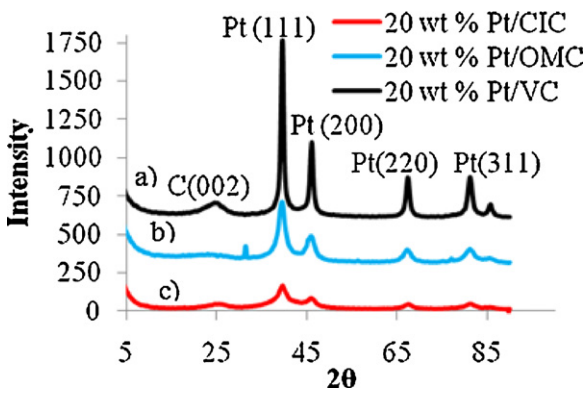

Fig. 4. XRD patterns of (a) VC, (b) OMC, and (c) CIC after 20 wt% Pt loading.

In Eq. (2), ΔG_f represents the free energy of formation of the reactants and products, while ΔG_{rxn} is the free energy of reaction (1). Amorphous carbon is known to have a more positive ΔG_f value than graphitic carbon [31] (this can also be deduced from the fact that graphite is the most thermodynamically stable allotrope of carbon, and thus has a ΔG_f value of 0 kJ mol^{-1}), making the oxidation of amorphous carbon more favourable than graphitic carbon. Aqueous electrochemical corrosion studies are currently underway to verify these preliminary TGA results, which suggest that the CIC support should be more resistant to oxidation than the OMC material.

Another significant conclusion that can be reached from Fig. 3 is that all three Pt/C catalysts have the same Pt loading, in this case, 20%. This is seen from the fact that the final masses of all of the catalysts are essentially the same (~20% of the original mass), as only Pt should remain after heat-treatment at high temperatures.

3.4. Size, location, and distribution of Pt particles on carbon support materials

Table 2 shows the results obtained from the BET analyses of the three carbon support materials after Pt loading. While the carbon pore diameters remain unchanged, the surface areas and pore volumes are all a little smaller than in the absence of Pt (Table 1). For the mesoporous carbons, this may be due to Pt particles deposting inside the structural pores of these materials, while for VC, this is more likely to result from Pt deposition between individual VC particles, thus blocking textural pores, as will be confirmed below by TEM analysis.

Fig. 4 shows the XRD patterns of the carbon samples after loading with 20 wt% Pt, with Table 2 giving the Pt particle sizes, calculated using the Scherrer equation. The VC support clearly generates the largest Pt crystallites (9 nm), consistent with the sharp Pt peaks seen in Fig. 4 for this sample. This is because VC has the lowest total surface area (Tables 1 and 2) and also as its micropores are not utilized for Pt deposition [26]. Thus, the available surface area is far less than the total BET surface area of 220 m^2 g^{-1}.

The OMC, with its very high surface area, would have been expected to result in the smallest Pt particle sizes. However, the observation (Table 2) that the average Pt particle size (4.5 nm) is similar to that on the CIC (3.5 nm) may be partly explained by the deposition of Pt only in the larger (3.3 nm) pores [7], which contribute only ~35% of the total surface area of the OMC material (Table 1). In fact, the 3.3 nm OMC pores may also not be fully accessible to the larger Pt nanoparticles, and thus only a fraction of the internal OMC surface area will be available for Pt deposition.

In order to verify the Pt particle sizes obtained using XRD (Table 2), TEM analysis was performed (Fig. 5). For the VC support, individual carbon particles 60–80 nm in size were observed (Fig. 5a). However, it is not possible to clearly resolve the pores in

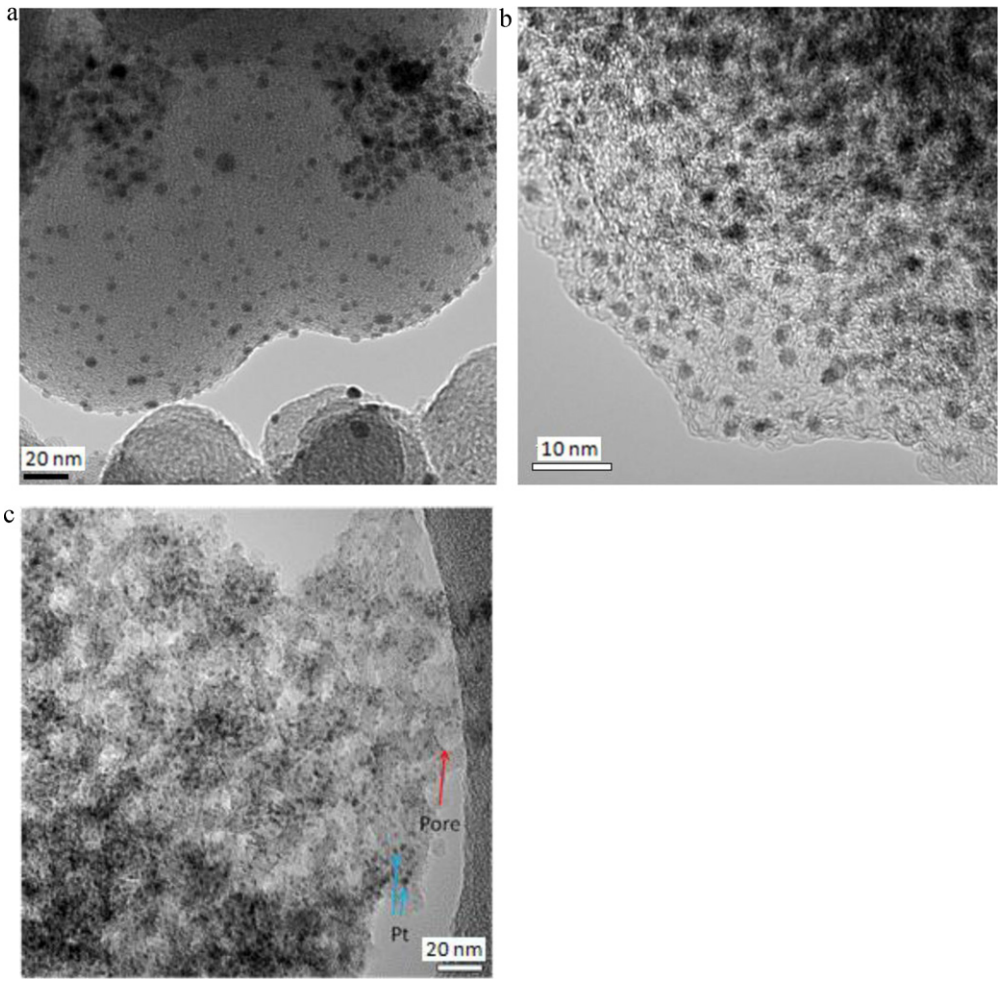

Fig. 5. Representative TEM images of 20 wt% Pt-loaded (a) VC, (b) OMC, and (c) CIC carbon support materials.

the VC material, which is not surprising, as our gas sorption studies have clearly indicated that VC is primarily microporous in nature (Tables 1 and 2), in agreement with the literature [25,26]. For the Pt/OMC (Fig. 5b), it is again not possible to discern the individual pores within the OMC support. This is consistent with the BET results (Tables 1 and 2), which show that these pores are relatively small (1.6 and 3.3 nm) and have a wormhole structure, with no long range order [7]. However, the pores in the CIC are clearly resolvable in Fig. 5c, being ~15 nm in diameter, in very good agreement with the BET results (Tables 1 and 2).

Fig. 5 also reveals the Pt particle sizes on the three carbon supports. On VC, a broad size distribution is seen (3–12 nm) and the Pt particles are clearly much larger than on the OMC and CIC supports, in agreement with the XRD results (Table 2). For the Pt/OMC and Pt/CIC materials (Fig. 5b and c, respectively), a narrower distribution of Pt nanoparticle size (2.5–4 nm) is observed than on VC, similar to what was obtained from the XRD data (Table 2). However, nothing can be concluded from Fig. 5 about the location of the Pt nanoparticles, i.e., whether they are located predominantly inside the pores or on the outer surface of the carbon particles. Therefore, 3D TEM and TEM electron tomography techniques were employed. It is important to note that tomograms (e.g., Fig. 6) are not conventional TEM images, and rather, are obtained from digital slices through the reconstructed 3D particles. Therefore, they can

Table 2
Selected physical properties of carbon supports after loading with 20 wt% Pt.

Carbon support	BET surface area ($\pm 10\ m^2\ g^{-1}$)	Pore size[a] (nm)	Pore volume ($mL\ g^{-1}$)	Pt crystallite size (± 0.5 nm) from XRD	Pt crystallite size range (nm) from TEM	Estimated Pt surface area[b] ($m^2\ g^{-1}$ Pt)	ECSA ($m^2\ g^{-1}$)[c] ($\pm 10\%$)
VC	170	<2.0	0.55	9	3–12	31 ± 2	39
OMC	1210	1.6, 3.3	0.84	4.5	2.5–3	62 ± 7	60
CIC	270	15	1.05	3.5	2.5–4	80 ± 11	65

[a] Calculated using the BJH (Barrett–Joyner–Halenda) model.
[b] Obtained by dividing the total volume of Pt in the catalyst layer (obtained from its mass) by the volume of one Pt nanoparticle (from the XRD radius), thus giving the total number of Pt particles. This was then multiplied by the surface area of 1 Pt nanoparticle and divided by the mass of Pt in the catalyst layer, giving $m^2\ g^{-1}$. Spherical Pt nanoparticles were assumed in this calculation.
[c] Electrochemical surface areas (ECSA) of mesoporous carbon supports are likely underestimated, due to difficulties in accounting for their large double layer charging (background) currents in CV experiments.

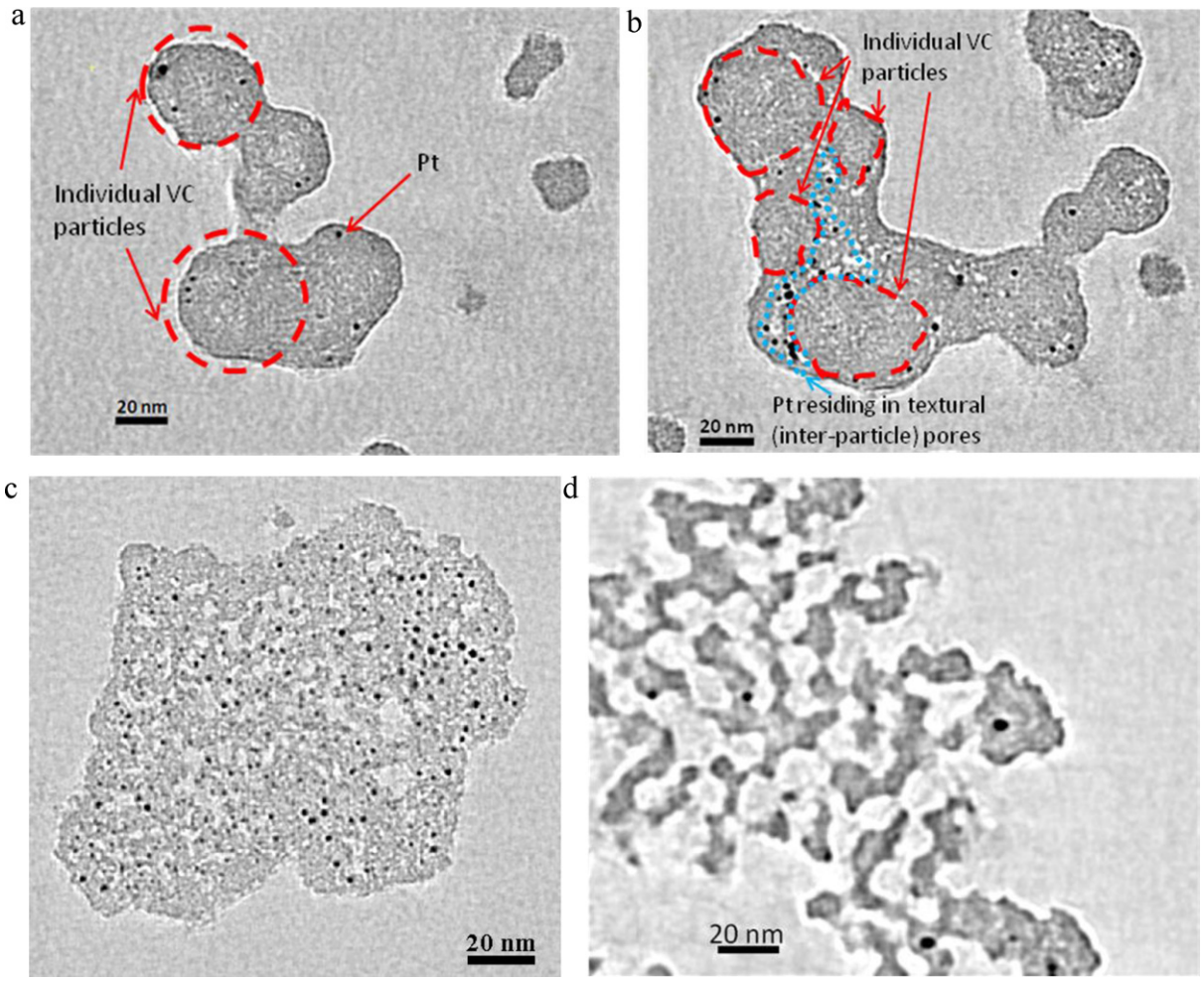

Fig. 6. Tomography slices through samples of 20 wt% Pt-loaded (a and b) VC, (c) OMC, and (d) CIC. In (a) and (b), individual VC particles are circled in a dashed red line, and in (b), Pt particles that are residing in the textural pores (between the VC particles) are circled in dotted blue lines. (For interpretation of the references to color in this figure legend, the reader is referred to the web version of the article.)

provide powerful information as to the location and size of the Pt nanoparticles as a function of depth into the carbon particles (and thus into the carbon pores).

For the tomographic analysis of Pt/VC (Fig. 6a and b), successive image slices through the sample confirmed that the majority of the Pt nanoparticles reside in what appear to be textural pores (pores between agglomerated VC carbon particles), as opposed to inside the framework porosity (pores within each VC particle). This is more clearly visible in the tilt series obtained for VC (Supplementary material). In some images, the deposited Pt particles are seen to trace the circumference of individual VC particles (Fig. 6b). Therefore, it is clear that the VC pores are too small (<2 nm) to accommodate Pt, resulting in the deposition of larger (3–12 nm) nanoparticles on the outer surface of the VC particles.

Fig. 6c shows the tomogram of the Pt/OMC. It is very clear from this snapshot that Pt has been deposited throughout the porous OMC network. This is a very important result, showing the most homogeneous distribution of Pt ever reported for this type of OMC material. However, based on the 2.5–3 nm size of the Pt particles, only the 3.3 nm pores can be utilized for Pt deposition and the 1.6 nm pores in OMC must therefore remain empty. The fact that only 35% of the OMC volume contains the 3.3 nm pores helps to explain why the Pt nanoparticle size is very similar at the OMC and CIC supports (Table 2).

Fig. 6d shows the tomographic image of the Pt/CIC catalyst, indicating that the Pt nanoparticles are uniformly distributed inside the 15 nm pores of the CIC support. This is the first reported tomogram of a CIC material, and it clearly shows that the internal porous volume of the CIC (light regions in Fig. 6d) is significantly larger than the OMC (light regions in Fig. 6c). It should be noted that the pores seen in Fig. 6 are 3-dimensional and thus it is not possible to conclude from these images whether the pores are closed or open, since a pore that appears to be closed in the $x-y$ direction is also extending in the z direction. A comparison of Figs. 6c and d also shows that the CIC has significantly thicker walls (5–10 nm) between the pores than does the OMC (1–3 nm), with this latter value matching closely with the expected wall thickness based on the pore size of the ordered mesoporous silica used to synthesize the OMC support [7]. Our recent work [18] has indicated that wall thickness may be an important factor in designing optimal catalyst supports, with thicker carbon walls providing better electronic conductivity of the catalyst layer. These results thus predict that the CIC support material will introduce less resistance into the catalyst layer than will the OMC.

3.5. ORR characteristics of Pt/C catalysts

For the comparison of the ORR activities at the three Pt-loaded carbon catalysts, 3-electrode techniques were chosen, as this approach eliminates performance-limiting contributions from the anode and electrolyte, encountered in single cell testing, as well as any differences that may arise during assembly of a full cell.

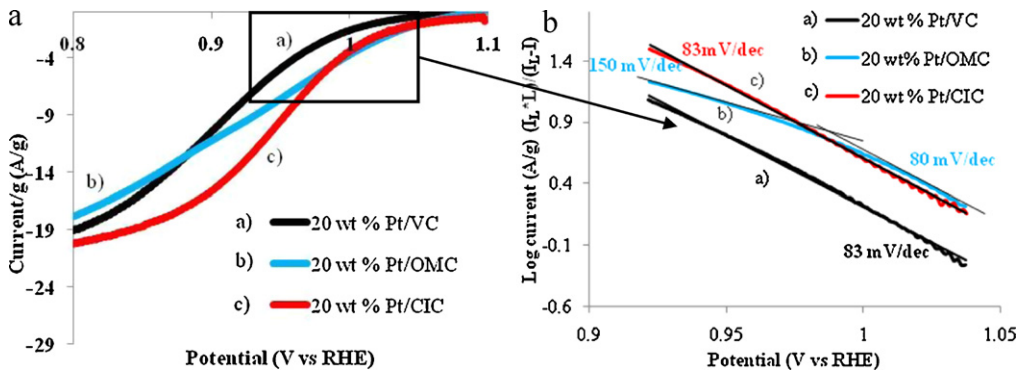

Fig. 7. (a) Oxygen reduction activity and (b) related Tafel plots for 20 wt% Pt-loaded VC, OMC and CIC at 10 mV s^{-1} and 1000 rpm in RT O_2-saturated 0.5 M H_2SO_4.

Therefore, Fig. 7a shows a comparison of the 3-electrode ORR characteristics of the Pt-loaded carbons on a rotating disc electrode, all for a 20 wt% Pt loading and at a constant electrode rotation rate of 1000 rpm, with Fig. 7b showing the Tafel plots of the low overpotential data. The currents in this range of potential are kinetically controlled, as seen by their lack of dependence on potential sweep rate or electrode rotation rate. This is also supported by the anodic ORR Tafel slopes of close to 80 mV $decade^{-1}$ of current (Fig. 7b, Table 3) that were observed for all three supports. This is a commonly reported value for the ORR at Pt/C catalysts in the anodic CV scan direction in RDE experiments [32]. Also, the cathodic Tafel slopes (not shown) were found to be close to the theoretical 60 mV $decade^{-1}$. Therefore, we are confident that the Tafel data in Fig. 7b are free from diffusional or migrational effects [33,34], at least until the onset of the bending in the plot at higher overpotentials (<~1 V), observed only for the Pt-loaded OMC support.

In the low overpotential (kinetic) region, it is clear from Fig. 7 that both of the Pt-loaded mesoporous OMC and CIC carbon supports give a significantly better ORR performance than does the Pt-loaded VC. These results (e.g., at 1.03 V, Table 3) show that the currents are ca. 3 times higher for the mesoporous supports than for VC, for both 20 and 40% Pt loadings. These results are trending in the same direction as predicted from the XRD and TEM data (Table 2), which showed that the Pt nanoparticles deposited on the two mesoporous supports are similar in size (3–4 nm), while the Pt particles on VC are significantly larger and less uniform (3–12 nm). Thus, the total surface area of Pt is expected to be higher on the OMC and CIC supports, and smaller on VC. In Table 3, the A g^{-1} values, in both the kinetic and mixed kinetic diffusion regions, are all smaller for the 40 wt% Pt loadings vs. the 20 wt% Pt loadings. This is expected, due to the larger Pt particle size reportedly obtained when higher Pt loadings are employed [8].

The Pt electrochemical surface area (ECSA) was calculated for the three catalysts from the hydrogen underpotential deposition (HUPD) charges (Table 2), giving values on the CIC and OMC supports of 60–65 m^2 g^{-1}, while, on VC, the ECSA is ~40 m^2 g^{-1}. As these differences in the measured ECSA values do not fully account for the factor of ~3 in activity between Pt/VC, and either Pt/OMC or Pt/CIC (Table 3), the Pt area was also calculated using the XRD data, assuming a spherical Pt particle shape. In fact, there is a significant error in the ECSA values for the mesoporous supports, due to their very large background capacitive currents, resulting in an underestimation of the active Pt surface areas. Table 2 shows that these Pt surface areas agree more closely with the ORR activity differences for the three carbon supports in Table 3.

Taken together, Figs. 6 and 7 demonstrate that a key advantage of both of the mesoporous carbon supports is their ability to better distribute the deposited Pt, hosting them inside the carbon pores, rather than just on the outer surfaces. This leads to smaller Pt particle sizes and thus a higher total Pt surface area, available for the ORR. It is also noteworthy that, while full Pt stability tests have not yet been performed, the ECSA values did not change during the timeframe of our experiments (~30 min with cycling between 0.05 and 1.1 V at 10 mV s^{-1}). This argues that the Pt nanoparticle size, shape, and distribution remained stable during the 3-electrode ORR activity evaluation.

Fig. 7 also demonstrates that the Pt-loaded VC and CIC can be polarized to higher overpotentials than can the Pt-loaded OMC without encountering mass transport limitations. The onset of bending of the Tafel plot (Fig. 7b) commences at ca. 1.01 V for Pt/OMC, but not until < 0.92 V for Pt/VC and Pt/CIC. The higher (~150 mV), but linear, Tafel slope observed for the Pt-loaded OMC at potentials < 1.01 V could have several origins. One is the predicted lower electronic conductivity of the OMC, arising from its relatively amorphous nature, as shown by the XRD and TGA results (Figs. 2 and 3, respectively). This may be exacerbated by the very thin walls (1–3 nm) of the OMC vs. the CIC (5–10 nm) support [18], observed in the TEM images in Fig. 6. The high Tafel slopes at Pt-OMC (Table 3) may also arise from mass transport limitations (of O_2, H^+, H_2O) to/from the Pt nanoparticles that are located deep

Table 3
Selected ORR characteristics at 20 and 40 wt% Pt-loaded carbons.

Carbon support	Pt loading (wt%)	Current at 1.03 V (A g^{-1}) (kinetic region)	Current at 0.9 V (mixed kinetic/mass transport region)	Tafel slope (>0.92 V) (mV $decade^{-1}$) ± 5 mV $decade^{-1}$
VC	20	0.55	10.5	83
OMC	20	1.8	13.0	80, 150[a]
CIC	20	1.8	16.5	83
VC	40	0.32	7.1	78
OMC	40	1.0	6.7	85, 140[a]
CIC	40	1.0	8.5	82

[a] Tafel slopes measured after the onset of bending in plots in Fig. 7b at <1.01 V.

within the mesopores. This would be much more prevalent for the OMC support, vs. CIC, as the Pt-containing pore diameters are only 3.3 nm for the OMC, compared to 15 nm for the CIC support. Long and narrow pores are known to lead to mass transport effects in porous electrodes [33,34], leading to higher Tafel slopes.

Both the low electronic conductivity and diffusional limitations within the OMC pores will cause a potential drop through the Pt/OMC catalyst layer, thus increasing the Tafel slope and lowering overall cathode performance [35,36]. The resulting poor ORR activity of the Pt/OMC material, particularly at high currents [12,13,37], is a major problem, as cathodes in PEM fuel cells typically operate at potentials of 0.5–0.9 V vs. RHE [38]. In contrast, the Pt/CIC catalyst maintains its excellent performance over the full potential range.

4. Conclusions

This work represents the first direct comparison between the properties of two classes of mesoporous carbons [a silica colloid-imprinted carbon (CIC) and a ordered mesoporous carbon (OMC) formed using a silica template] and those of a conventional microporous (<2 nm) carbon (Vulcan Carbon, VC) when employed as a Pt catalyst support for application as PEM fuel cell cathodes, all in a single study. BET analysis showed that the CIC pores are 15 nm in diameter, while the OMC has bimodal pores 1.6 and 3.3 nm in size. XRD analysis revealed that the CIC and VC supports both have a significantly more graphitic character than does OMC and thus should be both more conductive and more oxidation resistant, as confirmed by TGA analysis.

TEM electron tomography revealed the internal porous structure of the carbon supports and the precise location of the Pt nanoparticles at an unprecedented level. It was shown that, while Pt resides primarily on the outer surfaces of the microporous VC powder, the Pt nanoparticles are homogenously distributed throughout the 15 nm mesopores of the CIC and in the larger (3.3. nm) pores of the OMC supports. Both the OMC and CIC supports exhibited significantly better Pt nanoparticle dispersion and uniformity (2.5–4 nm) than did VC (3–12 nm). Also, the tomography revealed differences in the wall thickness of the mesoporous carbon supports, being 1–3 nm for the OMC and 5–10 nm for the CIC.

The three carbon supports, loaded with 20 and 40 wt% Pt, were evaluated for their oxygen reduction (ORR) activity on a glassy carbon rotating disc electrode in O_2-saturated 0.5 M H_2SO_4. At low overpotentials, both the Pt/OMC and Pt/CIC catalysts outperformed the Pt/VC catalyst, related primarily to the smaller size of the Pt particles (higher surface area) on the mesoporous carbon supports. However, at higher overpotentials, the performance of the Pt/OMC deteriorated significantly. This is attributed to restricted mass transport within the smaller pores of the OMC and a lower electronic conductivity, due to its less graphitic nature and thinner walls, vs. Pt/CIC. The results of this work strongly suggest that future work on mesoporous carbon supports for PEM fuel cell applications should focus on the highly promising CIC materials, rather than on the OMC supports.

Acknowledgements

We gratefully acknowledge Ballard Power Systems and the Natural Sciences and Engineering Research Council of Canada (NSERC) Strategic Research Project Program for the financial support of this work. We also thank Alberta Ingenuity, now part of Alberta Innovates-Technology Futures, and NSERC for the scholarship support of D.B., and Professors J. Hill and P. Pereira (University of Calgary) for access to N_2 sorption instrumentation. The authors also thank Jason Young for assistance with the TGA experiments, and Dr. Scott Paulson for many helpful discussions.

Appendix A. Supplementary data

Supplementary data associated with this article can be found, in the online version, at doi:10.1016/j.jpowsour.2011.02.034.

References

[1] K. Wikander, H. Ekström, A.E.C. Palmqvist, G. Lindbergh, Electrochim. Acta 52 (2007) 6848–6855.
[2] D.B. Spry, A. Goun, K. Glusac, D.E. Moilanen, M.D. Fayer, J. Am. Chem. Soc. 129 (2007) 8122–8130.
[3] T.D. Gierke, G.E. Munn, F.C. Wilson, J. Polym, Sci. Polym. Phys. Ed. 19 (1981), 1687-1170.
[4] H. Tang, Z. Qi, M. Ramani, J.F. Elter, J. Power Sources 158 (2006) 1306–1312.
[5] S. Lowell, J.E. Shields, M.A. Thomas, M. Thommes, Characterization of Porous Solids and Powders: Surface Area Pore Size and Density, 1st ed., Springer, Dordrecht, Netherlands, 2006.
[6] Z. Li, M. Jaroniec, J. Am. Chem. Soc. 123 (2001) 9208–9209.
[7] D. Banham, F. Feng, J. Burt, E. Alsrayheen, V. Birss, Carbon 48 (2010) 1056–1063.
[8] S.H. Joo, S.J. Choi, I. Oh, J. Kwak, Z. Liu, O. Terasaki, R. Ryoo, Nature 412 (2001) 169.
[9] H. Chang, S.H. Joo, C. Pak, J. Mater. Chem. 17 (2007) 3078–3088.
[10] K. Wikander, A.B. Hungria, P.A. Midgley, A.E.C. Palmqvist, K. Holmberg, J.M. Thomas, J. Colloid Interface Sci. 305 (2007) 204–208.
[11] N.P. Lebedeva, A.S. Booij, G.J. Janssen, ECS Trans. 16 (2008) 2083–2092.
[12] E. Ambrosio, C. Francia, C. Gerbaldi, N. Penazzi, P. Spinelli, M. Manzoli, G. Ghiotti, J. Appl. Electrochem. 38 (2008) 1019–1027.
[13] E.P. Ambrosio, C. Francia, M. Manzoli, N. Penazzi, P. Spinelli, Int. J. Hydrogen Energy 33 (2008) 3142–3145.
[14] E. Antolini, Appl. Catal. B 88 (2009) 1–24.
[15] C.H. Kim, D.K. Lee, T.J. Pinnavaia, Langmuir 20 (2004) 5157–5159.
[16] F. Su, C.K. Poh, Z. Tian, G. Xu, G. Koh, Z. Wang, Z. Liu, J. Lin, Energy Fuels 24 (2010) 3727–3732.
[17] B. Fang, J.H. Kim, J.-S. Yu, Electrochem. Commun. 10 (2008) 659–662.
[18] K. Pei, D. Banham, F. Feng, T. Fürstenhaupt, S. Ye, V. Birss, Electrochem. Commun. 12 (2010) 1666–1669.
[19] R. Ryoo, S.H. Joo, S. Jun, J. Phys. Chem. B 103 (1999) 7743–7746.
[20] D. Zhao, Q. Huo, J. Feng, B.F. Chmelka, G.D. Stucky, J. Am. Chem. Soc. 120 (1998) 6024–6036.
[21] D.N. Mastronarde, J. Struct. Biol. 152 (2005) 36–51.
[22] J.R. Kremer, D.N. Mastronarde, J.R. McIntosh, J. Struct. Biol. 116 (1996) 71–76.
[23] D.N. Mastronarde, J. Struct. Biol. 120 (1997) 343–352.
[24] T.A. Centeno, F. Stoeckli, Electrochim. Acta 52 (2006) 560–566.
[25] Y. Shao, J. Liu, Y. Wang, Y. Lin, J. Mater. Chem. 19 (2009) 46–59.
[26] H.I. Lee, S.H. Joo, J.H. Kim, D.J. You, J.M. Kim, J.-N. Park, H. Chang, C. Pak, J. Mater. Chem. 19 (2009) 5934–5939.
[27] S. Maass, F. Finsterwalder, G. Frank, R. Hartmann, C. Merten, J. Power Sources 176 (2008) 444–451.
[28] Z. Li, M. Jaroniec, Y.-J. Lee, L.R. Radovic, Chem. Commun. (2002) 1346–1347.
[29] K.P. Gierszal, M. Jaroniec, T.W. Kim, J. Kim, R. Ryoo, New J. Chem. 32 (2008) 981–993.
[30] A.B. Fuertes, T.A. Centeno, J. Mater. Chem. 15 (2005) 1079–1083.
[31] K. Jacob, S. Seetharaman, Metall. Mater. Trans. B 25 (1994) 149–151.
[32] S.L. Gojkovic, S.K. Zecevic, R.F. Savinell, J. Electrochem. Soc. 145 (1998) 3713–3720.
[33] R. de Levie, Electrochemical Response of Porous and Rough Electrodes, John Wiley & Sons, New York, 1967.
[34] M.L. Perry, J. Newman, E.J. Cairns, J. Electrochem. Soc. 145 (1998) 5–15.
[35] J.N. Soderberg, A.C. Co, A.H.C. Sirk, V.I. Birss, J. Phys. Chem. B 110 (2006) 10401–10410.
[36] D.W. Banham, J.N. Soderberg, V.I. Birss, J. Phys. Chem. C 113 (2009) 10103–10111.
[37] E.P. Ambrosio, M.A. Dumitrescu, C. Francia, C. Gerbaldi, P. Spinelli, Fuel Cells 9 (2009) 197–200.
[38] J.P. Meyers, R.M. Darling, J. Electrochem. Soc. 153 (2006) A1432–A1442.